

# Analysis of instantaneous profiles of intense femtosecond optical pulses propagating in helium gas measured by using femtosecond time-resolved optical polarigraphy

Masatoshi Fujimoto,\* Shin-ichiro Aoshima, Makoto Hosoda,† and Yutaka Tsuchiya

*Central Research Laboratory, Hamamatsu Photonics K. K., 5000 Hirakuchi, Hamakita City 434-8601, Japan*

(Received 8 April 2001; published 17 August 2001)

We analyze instantaneous profiles of intense femtosecond optical pulses propagating in helium gas measured using femtosecond time-resolved optical polarigraphy (FTOP). Considering the characteristics of the optical Kerr effect, relations linking images obtained by FTOP with intensity distributions of optical pulses are derived under approximations applicable to a relatively wide range of experimental conditions. By inversely applying the derived equations, images proportional to instantaneous intensity distributions of propagating light pulses are constructed from snapshot images taken in the experiment. From an analysis of the images obtained, we discuss the temporal changes in the optical-pulse profiles. We can directly observe the energy reduction of the optical pulses after they pass through the simultaneously generated laser plasma. It is confirmed that each filament can be separately investigated by this method even under multifilament conditions. Furthermore, the images clearly reveal intensity distributions along the propagation axis as well as cross-section distributions of femtosecond-pulse filaments, and show temporal shape modulations shorter than the incident pulse width in the middle of the propagation. We specify the volume where the light energy concentrates at a particular instant of time, and directly observe the cross-section expansion of the volume at the focal point brought about due to nonlinear effects.

DOI: 10.1103/PhysRevA.64.033813

PACS number(s): 42.60.Jf, 42.65.Re, 06.60.Jn, 42.25.Lc

## I. INTRODUCTION

Since light travels fastest in the universe, it would seem to be quite difficult to observe its instantaneous intensity distribution as it propagates. Normally, to know the intensity of light a detector has to receive the target light and represent the intensity distribution along the propagation axis of the light by the temporal change of the detector's signal. Indeed, when people say that light can be seen, they only state that light can be detected by their eyes, and do not mean that they can recognize the shape of the light at a specific instant. Sometimes, however, it is convenient to regard the intensity of light as a three-dimensional object with a distribution that changes as time passes. Examples include the case of intense femtosecond optical pulses propagating in some medium. The distributions of these pulses are localized along their propagation axis. Furthermore, their light path changes and becomes significantly different from the path expected by linear optics due to self-modulating nonlinear effects, and the intensity is localized to form an optical filament [1–4]. Therefore, the energy is concentrated in regions having linear dimensions of less than submillimeter order, and the profiles vary from time to time [4–7]. Observing the instantaneous light profiles is particularly important in cases like this, i.e., when the light intensity becomes large enough to make the propagation nonlinear. Of course, this is also a very fascinating subject from the viewpoint of fundamental science.

Recently, we proposed and demonstrated a measurement

method called femtosecond time-resolved optical polarigraphy (FTOP), which catches the light intensity distribution as a spatial profile at a particular instant of time [8]. This method makes use of the birefringence induced by the electric field of the intense laser pulse to be measured, and visualizes a light pulse with the femtosecond temporal window of the optical probe pulse. Hence, FTOP can be considered to be one method for following and observing the temporal changes of instantaneous intensity distributions of optical pulses, and can enable an examination of the nonlinear propagation dynamics of intense laser pulses.

In this paper, we construct the theoretical foundation of FTOP images under several appropriate approximations in order to reveal how the intensity distributions are obtained from the images taken in the experiment as well as to justify our experimental conditions. Making use of the equations obtained, we investigate snapshot images of intense femtosecond optical pulses propagating in helium gas, and directly show their complicated behaviors due to nonlinear propagation. In particular, we discuss the alteration of the pulse width, which is estimated from an image. Observations with this method can contribute toward an understanding of the mechanism of filament formation involving femtosecond pulses.

## II. THEORY

In isotropic media, there is no second nonlinear term, and therefore the third nonlinearity is dominant. We show that this third nonlinearity, especially the optical Kerr effect, can be utilized for the visualization of instantaneous pulse profiles under several ordinary assumptions.

### A. Arrangement and several assumptions

As shown in Fig. 1, consider that the intense light pulse to be measured, named the pump pulse, is propagating along

\*Electronic address: fujimoto@crl.hp.k.co.jp

†Present address: Faculty of Engineering, Osaka City University, 3-3-138 Sugimoto, Sumiyoshi Osaka 558-8585, Japan.

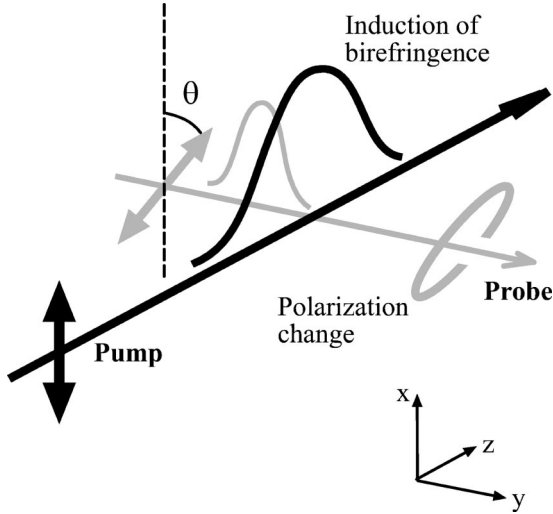


FIG. 1. Illustrating the pump-probe arrangement of FTOP. The one-way arrows indicate the propagation directions of the pulses. Both pulses are linearly polarized, and the directions of the vibrations of their electric fields are indicated by the round-trip arrows. The anisotropic change of the refractive index is induced by the pump pulse according to its intensity distribution. The probe pulse senses the birefringence, and its polarization state is altered. The amount of probe-polarization change reflects the instantaneous intensity distribution of the pump pulse.

the  $z$  axis in an isotropic medium. The pump pulse is linearly polarized with its electric field in the  $x$  direction. Also consider that a probe pulse is introduced, which propagates along the  $y$  axis. The probe pulse is sufficiently weak and has a linear polarization of angle  $\theta$ , which represents the direction of its electric field from the  $x$  axis in the  $xz$  plane. The frequency components of each pulse are assumed to be approximated to a representative value, and this can be done when the frequency width is narrow enough so as not to change how the medium responds. This approximation is appropriate at least for a response originating from electronic motion without resonance, provided that the widths of the pulses employed are more than several tens of femtoseconds. (The validity of this approximation is discussed in Sec. II E.) Although the representative frequencies can differ between the pump and probe, we use the same value here and express the angular frequency as  $\omega$  in order to match our experimental conditions.

For simplicity, absorption of any type is assumed to be negligible at the frequency considered, and this assumption permits the linear and nonlinear susceptibility components to be treated as real parameters. As usual, there is no need to use the linear susceptibility  $\chi^{(1)}(-\omega; \omega)$  itself after the permittivity (which is also real) is defined as  $\epsilon(\omega) = \epsilon_0[1 + \chi^{(1)}(-\omega; \omega)]$ , where  $\epsilon_0$  is the vacuum permittivity.

When the pump intensity is large enough to make the nonlinear response of the medium significant, both pulses are influenced by the pump intensity due to the optical Kerr effect. Other effects, such as third harmonic generation, are not considered at this time. The probe pulse is considered to be weak enough that we can neglect effects due to not less than the second order of its electric field.

The dispersion relation of each pulse is obtained by retaining only the terms that correspond to propagation in each direction with angular frequency  $\omega$  [9,10]. From this procedure, a well known fact is derived, i.e., the pump pulse experiences the refractive index as  $n = n_0 + n_2 I(\mathbf{r}, t)$ , where  $I(\mathbf{r}, t)$  is the pump intensity at position  $\mathbf{r} = (x, y, z)$  and at time  $t$ . The coefficients are expressed as  $n_0 = \sqrt{\epsilon(\omega)/\epsilon_0}$ ,  $n_2 = [3/4c\epsilon(\omega)]\chi_{1111}^{(3)}(-\omega; -\omega, \omega, \omega)$ , where  $c$  is the vacuum velocity of light and  $\chi^{(3)}$  is the third nonlinear susceptibility tensor expressed in the usual definition [10–12]. On the other hand, the probe pulse experiences refractive index changes that differ between the electric field components along the  $x$  and  $z$  axes, i.e., induced birefringence. The refractive indices are expressed as

$$n_{\parallel} = n_0 + n_{2\parallel} I(\mathbf{r}, t)$$

$$\left( n_{2\parallel} \equiv \frac{3}{2c\epsilon(\omega)} \chi_{1111}^{(3)}(-\omega; -\omega, \omega, \omega) = 2n_2 \right), \quad (1)$$

$$n_{\perp} = n_0 + n_{2\perp} I(\mathbf{r}, t)$$

$$\left( n_{2\perp} \equiv \frac{3}{2c\epsilon(\omega)} \chi_{1221}^{(3)}(-\omega; -\omega, \omega, \omega) \right), \quad (2)$$

where  $\parallel$  and  $\perp$  indicate the amounts of  $x$  and  $z$  components of the probe electric field, which correspond to components parallel and perpendicular to the pump electric field, respectively [10–12].

Although an inhomogeneous refractive index induced by the pump may refract or diffract the probe pulse, we neglect these effects for simplicity, and the probe pulse is assumed to propagate straight along the  $y$  axis. Although the probe light is actually diffracted, the zero order diffracted component is dominant and travels almost completely along this approximate path [13]. Hence, the foregoing assumption is appropriate as the zero order approximation. (Of course, imaging lenses are needed for the profile detection in an actual experiment since the large distance between the pump path and the detection camera magnifies the distortion due to the probe diffraction.) On the other hand, in the case of the Schlieren method, which produces images of refractive index gradients, since the zero order diffracted component must be cut, the above simple processing is not allowed, thereby complicating the image analysis.

## B. Polarization change of the probe pulse

Since the refractive index varies in each place according to the pump pulse distribution, the phase of the probe electric field after interaction must contain the integral of the pump intensity. That is,

$$E_x(\mathbf{r}, t) = \frac{\mathcal{E}(\mathbf{r}, t) \cos \theta}{2} \exp \left[ i \left( \frac{n_0 \omega}{c} y - \omega t + \frac{\omega}{c} n_{2\parallel} \int_{-\infty}^y I(\mathbf{r}', t(\mathbf{r}')) dy' \right) \right] + \text{c.c.}, \quad (3)$$

$$E_z(\mathbf{r}, t) = \frac{\mathcal{E}(\mathbf{r}, t) \sin \theta}{2} \exp \left[ i \left( \frac{n_0 \omega}{c} y - \omega t \right) \right] + \frac{\omega}{c} n_{2\perp} \int_{-\infty}^y I(\mathbf{r}', t(\mathbf{r}')) dy' \Big] + \text{c.c.}, \quad (4)$$

$$w = w_0 \sin^2 \left[ \frac{\omega}{c} \frac{\Delta n_2}{2} \int I(\mathbf{r}', t(\mathbf{r}')) dy' \right] \approx w_0 \left( \frac{\omega \Delta n_2}{2c} \right)^2 \left[ \int I(\mathbf{r}', t(\mathbf{r}')) dy' \right]^2; \quad (7)$$

where  $\mathcal{E}(\mathbf{r}, t)$  is the envelope function of the incident probe electric field under the slowly varying envelope approximation at position  $\mathbf{r}=(x, y, z)$  and at time  $t$ .  $t(\mathbf{r}')$  represents the time when the probe arrives at position  $\mathbf{r}'=(x, y', z)$ , that is,  $t(\mathbf{r}')=t-(y-y')/v_g$ , where  $v_g$  is the group velocity of the probe pulse, i.e., the propagation velocity of the modulation. c.c. represents the complex conjugate of each leading term.

Extraction of the polarization change due to interaction can be done by using a polarization analyzer. Since we want to take images with the usual charge-coupled device (CCD) camera, no offset optical signal is desired in order to achieve a large dynamic range. Therefore, the direction of the analyzer is made to be perpendicular to that of the incident probe polarization. Hence, only the component of the probe field along the  $\theta + \pi/2$  axis in the  $xz$  plane,

$$-E_x \sin \theta + E_z \cos \theta = \frac{\mathcal{E}}{2} \exp \left[ i \left( \frac{n_0 \omega}{c} y - \omega t \right) \right] \times \sin 2\theta \frac{\exp(ib) - \exp(ia)}{2} + \text{c.c.}, \quad (5)$$

arrives at the detector, where the notations

$$a = (\omega/c) n_{2\parallel} \int I(\mathbf{r}', t(\mathbf{r}')) dy',$$

and

$$b = (\omega/c) n_{2\perp} \int I(\mathbf{r}', t(\mathbf{r}')) dy'$$

are used to simplify the expressions. Under the experimental condition that the analyzer is put sufficiently far from the pump propagation axis, the integrals should be performed over a region where  $I$  is nonzero. Since the detector senses the light energy, we should instead consider the probe intensity passing through the analyzer. This can be expressed as

$$w = \frac{1}{2} \sqrt{\frac{\epsilon}{\mu_0}} \mathcal{E} \exp \left[ i \left( \frac{n_0 \omega}{c} y - \omega t \right) \right] \times \sin 2\theta \frac{\exp(ib) - \exp(ia)}{2} \Big|^2 = w_0 \sin^2 2\theta \sin^2 \frac{a-b}{2}, \quad (6)$$

where  $w_0$  is the light intensity of the incident probe. From Eq. (6), it is easy to understand that the condition  $\theta = \pi/4$  is the most sensitive. In this condition, putting  $\Delta n_2 = n_{2\parallel} - n_{2\perp}$ , the probe intensity arriving at the detector is given by

this approximation holds when  $(\omega \Delta n_2 / 2c) \int I(\mathbf{r}', t(\mathbf{r}')) dy'$  is sufficiently small. In our experiment (described later), it was confirmed from the maximum of this value that this approximation is valid compared to the precision of the experiment. The estimation of this maximum value is described at the end of Sec. IV D.

### C. Image of pulse intensity distribution

Since  $w$  has an  $(x, z)$  dependence corresponding to the pump pulse intensity, it is easy to take pump intensity images when the detection is performed by, for example, a CCD camera. The CCD chip should be put parallel to the  $xz$  plane, and the images taken should be given by the brightness distribution in that plane. To get the expression for a detected image, the incident probe intensity is assumed to be homogeneous in the  $xz$  plane, and  $w_0 = G(t - y/v_g)$ . Then, the detected image, which corresponds to the probe fluence passing through the analyzer rather than the probe intensity, is given by substituting  $w_0$  into Eq. (7) and integrating all temporal contributions. Since we can control the incident time delay  $\tau$  between the pump and the probe, the image can be expressed as

$$W(x, z, \tau) = \int dt w = \left( \frac{\omega \Delta n_2}{2c} \right)^2 \int dt G(t) \times \left[ \int dy' I(x, y', z, t + \tau + y'/v_g) \right]^2. \quad (8)$$

When the pulse width of the probe is short compared to that of the pump, the simple relation

$$\int dy' I(x, y', z, \tau + y'/v_g) \propto \sqrt{W(x, z, \tau)} \quad (9)$$

is derived. Although the expression includes the integral of  $I$  along the  $y$  direction, we can see that the instantaneous intensity distribution of the pump pulse is surely captured. Here, we should note that an integral along the temporal direction only means coupling with the  $y$  direction and does not mean that the image comes to express the time-integrated profile. This will be discussed later.

In our experimental conditions, however, the incident pump and probe have the same pulse widths. Hence, the probe pulse width cannot be neglected and we should proceed to get the relation excluding the probe temporal profile. This is achieved by the usual deconvolution procedure. To see the explicit relation excluding the probe profile, we define the Fourier transformed amounts as

$$\tilde{W}(x, \xi, \tau) \equiv \int dz W(x, z, \tau) \exp(-iz\xi), \quad (10)$$

$$\tilde{G}(\xi) \equiv \int v_g dt G(t) \exp(-iv_g t \xi). \quad (11)$$

For simplicity, the pump pulse is assumed to propagate parallel to the  $z$  axis without changing its shape. This assumption is not necessary if the observations are performed with small delay steps, which demands a vast amount of image data. In the experiment described later, this assumption is not exactly true, but is thought to be reasonable if the region of the image taken is limited. Furthermore, the velocity of the pump pulse may be set to a constant value; this is true in our experimental conditions. Since our experiment adopts the same wavelength for the pump and the probe, this constant value should be  $v_g$ . Under these assumptions, the pump intensity can be expressed by using another function as

$$I(x, y, z, t) = \hat{I}(x, y, z - v_g t). \quad (12)$$

From Eqs. (8), (10), (11), and (12), the relation

$$\begin{aligned} & \int dy' \hat{I}(x, y', z - v_g \tau - y') \\ &= \frac{2c}{\omega |\Delta n_2|} \\ & \times \left[ \frac{v_g}{2\pi} \int d\xi \{ \tilde{W}(x, \xi, \tau) / \tilde{G}(\xi) \} \exp(iz\xi) \right]^{1/2} \end{aligned} \quad (13)$$

is obtained. In the actual calculation, however, to avoid the amplification of high-frequency noise, we do not use this explicit expression, but use a specified algorithm: a Bayesian deconvolution procedure [14]. After this procedure is applied to Eq. (8), the value of the left hand side of Eq. (13) is derived by extracting the square root of the deconvoluted result. Later, the function  $V(x, z, \tau)$  is defined as  $\int dy' \hat{I}(x, y', z - v_g \tau - y')$  multiplied by a certain constant factor as a matter of convenience.

We shall comment on the obtained image. The integral along the  $y$  direction means that the image is a projection onto the plane parallel to the detector, and this is common for each case of image detection. However, since the information obtained is expressed as  $\int dy' I(x, y', z, \tau + y'/v_g)$ , one might suspect that an integral variable also appears in the argument for the time dependence of the integrand. Exactly speaking, this expression is general for any imaging, but  $y'/v_g$  is usually neglected since the usual material does not move appreciably on that time scale. In our situation, however, the object is light and travels as fast as the probe does, and hence  $I$  significantly changes in the time  $y'/v_g$ , and the change cannot be neglected. Note that this does not mean time integral but coupling between the spatial and temporal directions, and therefore the image obtained can express the instantaneous profile of the light pulse.

To clarify, consider the situation where the pump intensity distribution is narrow for the  $y$  direction around the  $y=0$  plane. Under this condition, since the integrand contributes only around  $y'=0$  in the  $y'$  integral, the image obtained

roughly corresponds to  $I(x, 0, z, \tau)$ , which means the  $xz$  distribution at some instant  $\tau$ . On the other hand, in the situation that the pump intensity distribution is narrow for the  $z$  direction, the image obtained expresses the cross section of the pump beam. To see this explicitly, we restrict our consideration to within parallel propagation in the  $z$  direction. At this time, the integrand contributes only around  $y' = z - v_g \tau$  to the integral  $\int dy' \hat{I}(x, y', z - v_g \tau - y')$ , and therefore the image obtained corresponds to  $\hat{I}(x, z - v_g \tau, 0)$ . That is, the  $y$  axis of the object is completely converted into the  $z$  axis in the image. When the pump propagation is not exactly parallel, the image becomes distorted from the real cross-sectional profile. In an actual experiment, the characteristic of the pump intensity distribution is usually intermediate between these extreme cases. Later, to analyze the data obtained, we adopt the assumption that the pump profiles along the  $y$  and  $z$  directions are both Gaussian and that each relative shape is independent of the position along the other axis. Then, the  $z$  profile of the image also becomes a Gaussian shape with a variance equal to the sum of the individual variances. From this relation, it is easy to investigate the intensity-distribution width of the pump pulse at a particular instant of time even along its propagation axis, which is usually expressed in terms of the temporal width of the pulse.

#### D. Consideration of higher-order nonlinearities

Terms not less than the quadratic order of  $\chi^{(3)}$  or further nonlinear responses corresponding to the coefficients  $\chi^{(5)}, \chi^{(7)}, \dots$  may add other terms to Eqs. (1) and (2), which are proportional to  $I^2, I^3, \dots$  [12]. These extra terms modify the integrand of the  $y'$  integral in the preceding equations, i.e., they introduce terms proportional to  $I^2, I^3, \dots$  into the integrand. Generally, these terms should not be omitted, and the resulting equations should also include them. Therefore, the images obtained have more complex meanings than those expressed by Eqs. (8) or (9). Under the approximation that the pump intensity distribution has a Gaussian profile independently along each coordinate axis, this modification means that an image corresponding to the right hand side of Eq. (13) is a superposition of Gaussian profiles with widths in the ratio of  $1:1/\sqrt{2}:1/\sqrt{3}:\dots$  and with weights corresponding to the coefficients of the terms  $I, I^2, I^3, \dots$  on the left hand side of the modified Eq. (13). By considering the experimental results given below, however, the terms  $I^2, I^3, \dots$  do not seem appreciable because most of the profiles are well approximated by single Gaussian curves. Indeed, there are some images able to approximate not single Gaussians but the sums of two Gaussians. However, each pair of Gaussians has a ratio of widths that differs from those of other pairs, and this means that the double Gaussians are not caused by the contributions of higher-order nonlinear terms but represent the actual distributions. Therefore, in our experimental conditions, we can state that only the  $I$ -linear term contributes to the images, and that Eq. (13) can be applied without modification to the analysis of the images obtained.

### E. Consideration of time resolution due to the finite response time of media

Leading up to the equations in this section, we neglect the frequency dependence of the susceptibilities. In reality, however,  $\chi^{(1)}$  and  $\chi^{(3)}$  depend on the individual frequencies of their arguments, and this frequency dependence gives rise to the finite response time, particularly a longer decay time, of the optical Kerr effect [9,12,15]. This effect limits the time resolution of FTOP images, making each image of a pump intensity distribution elongated toward the pump propagation direction.

Let us consider the case of the experiment described below. We adopted pulses with a wavelength of around 800 nm and a width of about 100 fs, and observed their behaviors when they were propagating in helium gas. With helium, nothing but electronic motion contributes to third nonlinear interaction with light. It is known that the response time of the optical Kerr effect should be less than about several femtoseconds when induced by electronic motion without resonance [9,12,16]. Since this finite response time contributes to images only through convolution, the elongation effect for 100-fs pulses is estimated to be less than 1% compared with the pulse width; therefore, a femtosecond time resolution can be accomplished in principle. This response time is neglected in our experiment because there are factors giving larger errors. This statement holds for media in which the optical Kerr response originates only or predominantly from non-resonant electronic motion. In addition, although a molecular response originating from atomic motion is generally slow compared to the pulse width of 100 fs, this effect may sometimes be treated separately from the instantaneous response. For example, in the case of air, if the echo components are out of the detection range, the optical Kerr response is considered to be instantaneous [16,17].

Conversely, from the above discussion, an approximation neglecting the frequency dependence of  $\chi^{(3)}$  is considered to be appropriate under our experimental conditions, and this fact ensures the validity of the relations obtained. However, if we use much shorter pulses or prepare media having a larger frequency dependence of the susceptibilities, the equations derived in this section no longer hold, and femtosecond time resolution may not be ensured. For example, if liquid carbon disulfide is used as a medium, the time resolution should be about 1–2 ps [15,16,18]. At such times, we need a more refined theoretical consideration to interpret FTOP images.

### III. EXPERIMENTS

Figure 2 shows the top view of the experimental setup. The coordinate axis is set to correspond to the equations in the previous section. A Ti:sapphire amplifier system generates linearly polarized intense optical pulses, with their electric fields in the horizontal plane, of 800-nm central wavelength with a 10-Hz repetition rate. The temporal full width at half maximum (FWHM) of the pulses is 95 fs; this was confirmed by a single-shot autocorrelator assuming that the pulse shape was the square of the hyperbolic secant. To maintain consistency with the previous formulation, we

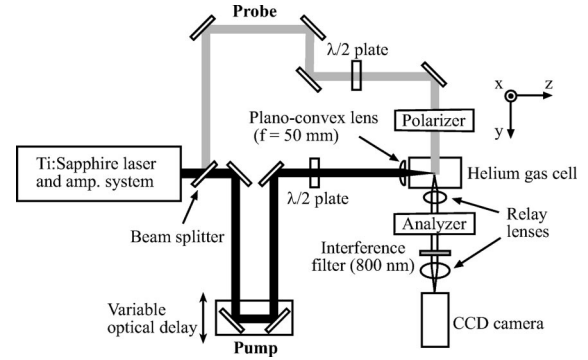


FIG. 2. Experimental setup of FTOP. The beam from the laser system is split into a pump and a probe. The pump, with an electric field redirected along the  $x$  axis, is focused in the quartz cell filled with helium gas. The probe is synchronously irradiated into the cell, and experiences the induced refractive index change due to the large electric field of the pump. To extract the pump intensity information effectively, the direction of vibration of the probe's electric field is shifted to an angle of  $\pi/4$  with the  $x$  axis in the  $xz$  plane, and the electric-field component perpendicular to the incident one is extracted by the analyzer after interacting with the pump-induced birefringence. The passed-probe component is detected by the CCD camera with a relay lens, in order to get images of the instantaneous intensity distribution of the pump.

choose helium gas as the medium the pump propagates through. To induce a sufficient optical Kerr effect even in helium gas, we carried out the experiment at a pulse energy in the millijoule region (gigawatt region peak power).

The beam output from the Ti:sapphire laser is split into a pump and a probe by a beam splitter. The pump beam carries most of the incident beam's energy. After passing through a variable optical delay, the polarization of the pump is changed as its electric field is along the  $x$  axis by the  $\lambda/2$  plate, and is then focused into the quartz cell filled with the helium gas by a 30-mm diameter planoconvex lens of  $f = 50$  mm. The lens diameter is larger than the cross section of the pump pulse, which has a whole diameter of about 20 mm, and the  $1/e$  diameter is 12.8 mm. The quartz cell is  $30 \times 30 \times 50$  mm<sup>3</sup> and it holds the helium gas at 1 atm and at room temperature. The probe pulse's polarization is also rotated by  $\pi/4$  by the other  $\lambda/2$  plate. Furthermore, although its electric field already makes an angle of  $\pi/4$  with the  $x$  axis in the  $xz$  plane after being reflected by a mirror, a polarizer is used to achieve a more precise linearity of the polarization along the same direction. Then, it is irradiated into the quartz cell as it crosses with the pump pulse. After interaction with the pump pulse through the medium and passing through the objective lens, the probe pulse enters the polarization analyzer, which selects the  $-\pi/4$  direction component of the electric field. Therefore, all unchanged probe components are cut here. An 800-nm interference filter is set in order to reduce the emission light from the plasma induced by the intense pump pulse. Finally, the passed-probe components are focused onto the CCD chip by using the imaging lens.

Under this arrangement, if the pump pulse is in the field of view of the imaging system when the probe pulse arrives

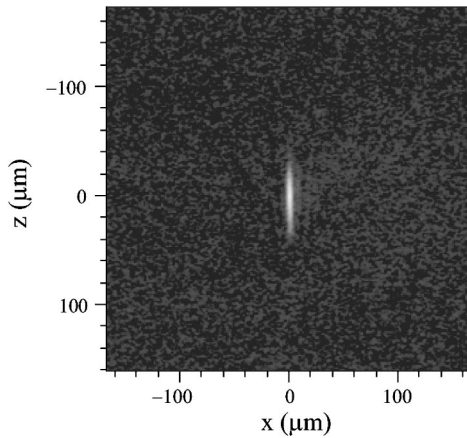


FIG. 3. FTOP image of a 0.53-mJ pulse propagating in helium gas. The optical pump pulse, which is the object of the image, propagates from top to bottom. The ordinate and the abscissa are the  $z$  and  $x$  axes, respectively. The origin is determined to coincide with the peak of the image, and this position gives a rough estimation of the vacuum focal point.

at the pump propagation axis, the probe components passed through the analyzer create the image of the pump-intensity distribution at the instant when the probe meets the pump, as written in the previous section. This timing is easily controlled by the variable optical delay set in the pump path. All plasma-emission and leaked-probe images, which are included in the raw image, can be removed by subtracting them after taking both of them separately. A FTOP image is constructed after this subtraction, and includes nothing more than a pump-probe interaction profile. The observed image is integrated over 10 shots to improve the signal-to-noise ( $S/N$ ) ratio, which is permitted since they are confirmed to be stable on a shot-to-shot basis. The scale of the images taken (shown later) is  $1.30 \mu\text{m}/\text{pixel}$ , which is fine enough compared with the spatial resolution of the images,  $3.0 \mu\text{m}$ , estimated from the numerical aperture of the objective lens.

The pump-propagation dynamics can easily be seen by changing the position of the variable optical delay. However, this procedure is not so suitable since the position of the pump pulse at the instant when it meets the probe pulse is immediately beyond the field of the imaging system. Hence, instead of a variable optical delay, we move the focusing planoconvex lens along the pump propagation axis. This always keeps the image lying around the center of the field. Although this method does not exactly monitor the same propagation on account of the pump beam diameter being altered at the incidence window of the cell, it does enable us to carry out observations over a long delay range with a large magnification. It was confirmed in our experimental conditions that moving the lens does not perceptibly change the manner of the pulse propagation. Since it is desirable to discuss the propagation dynamics in the situation that the focusing lens is fixed, the delay times and the  $z$  axes displayed below with the corresponding images are described with values as if the variable optical delay is moved by an amount that corresponds to the displacement of the focusing lens.

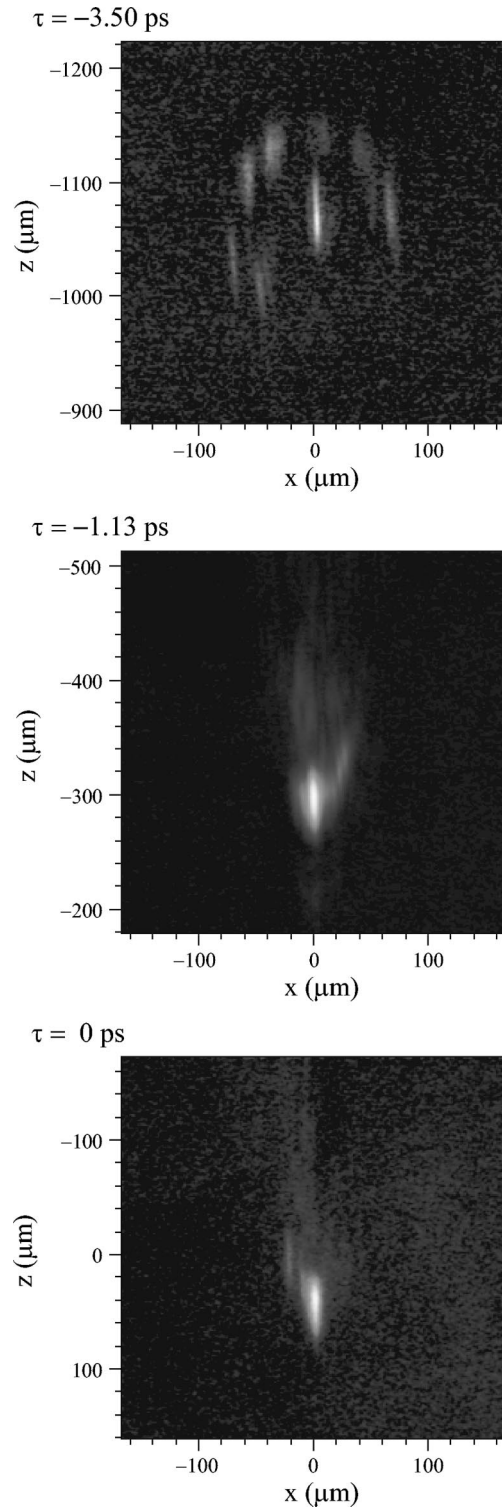


FIG. 4. FTOP images of a 13-mJ pulse propagating in helium gas. The time delay  $\tau$  from the image of Fig. 3 is indicated at the top of each image. The ordinate and the abscissa are the  $z$  and  $x$  axes, respectively. The origin of the  $xz$  plane is taken to be consistent with that of the 0.53-mJ image. The maximum brightness values of the images at  $\tau = -3.50$ ,  $-1.13$ , and  $0$  ps are 1.08, 10.24, and 2.03, respectively, provided that of Fig. 3 is unity. To make each profile clear, however, each image is normalized by its peak value.

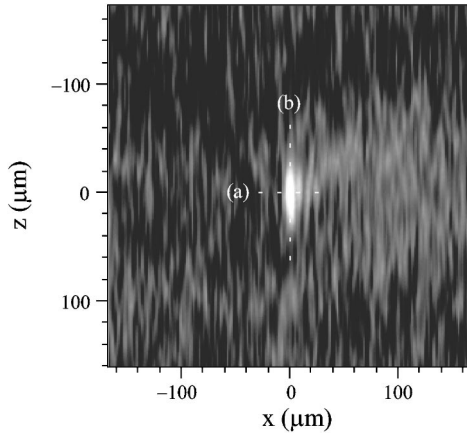


FIG. 5. Image of the function  $V(x, z, \tau=0)$  of a 0.53-mJ pulse. The image is constructed by deconvoluting the image in Fig. 3 with the probe pulse wave form and extracting the square root of each pixel. The origin of the  $xz$  plane is taken to be consistent with those of Figs. 3 and 4. Lines (a) and (b) reveal the segments along which the profiles are investigated and displayed in Fig. 7.

#### IV. RESULTS AND DISCUSSION

##### A. FTOP images obtained

In this section, some typical images are displayed in detail.

Figure 3 shows a FTOP image of a 0.53-mJ (4.9-GW peak power) pump pulse propagating in helium gas. The abscissa and the ordinate are the  $x$  and  $z$  coordinates, respectively. Hence, the pump pulse propagates from top to bottom in the image. The image adopted in Fig. 3 is the brightest one in a sequence obtained by changing the position of the focusing lens, and corresponds to an observation with the pump pulse at the vacuum focus. Under this energy condition, the observed images have a simple structure; they are cylindrically symmetric with respect to a central line parallel to the  $z$  axis at almost the same place in the field of view throughout the consecutive displacements of the focusing lens. The plasma induced by the pump pulse can also be observed and its emission, which is weak under this condition, covers the region  $-3 \times 10 \mu\text{m} < x < 5 \times 10 \mu\text{m}$ ,  $-9 \times 10 \mu\text{m} < z < 8 \times 10 \mu\text{m}$ .

Figure 4 shows FTOP images of a 13-mJ (0.12-TW peak power) pump pulse. As in Fig. 3, the pump light propagates from top to bottom in these images. The time delay  $\tau$  from the image of Fig. 3 is indicated at the top of each image. The coordinate axes are consistent with those in Fig. 3. The maximum brightness values of the images at  $\tau = -3.50$ ,  $-1.13$ , and  $0$  ps in Fig. 4 are 1.08, 10.24, and 2.03, respectively, provided that of Fig. 3 is unity. Under this energy condition, it is easily seen from the images and their maximum values that the pump pulse first produces a multifilament structure, then the filaments come together, and finally the pulse loses its energy as it propagates to be focused. At around  $\tau = -3.50$  ps, there are several filaments. This structure comes from the local self-focusing of the pump beam due to its intensity inhomogeneity [2,19]. This inhomogeneity is thought to originate from the laser light source and not from

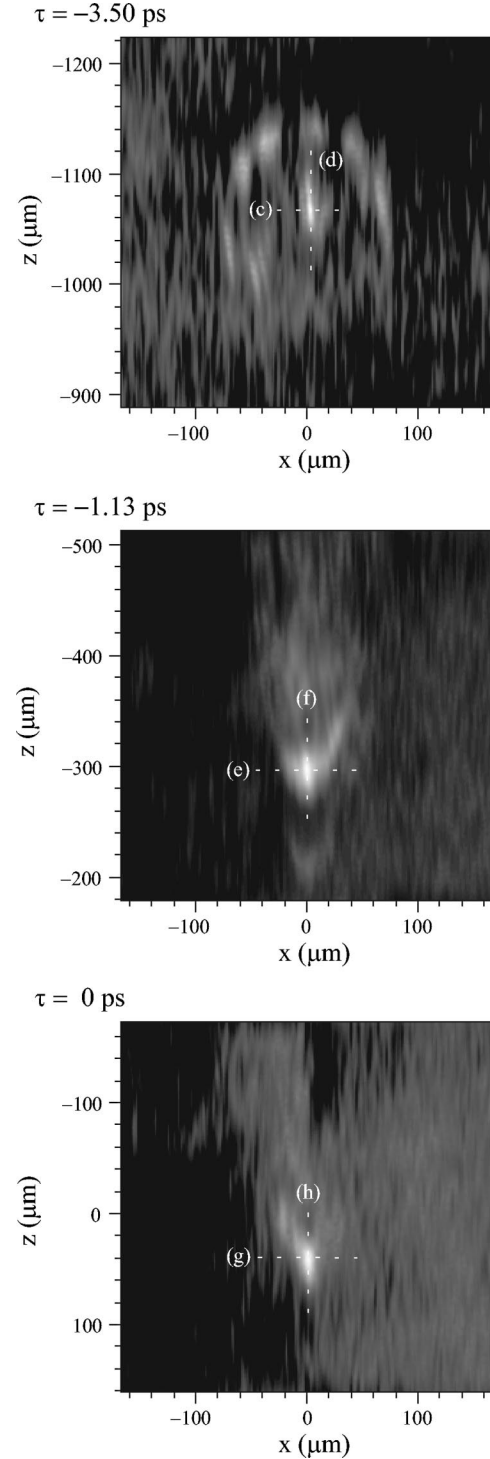


FIG. 6. Images of the function  $V(x, z, \tau)$  of a 13-mJ pulse. The images are constructed by deconvoluting the images in Fig. 4 with the probe pulse wave form and extracting the square root of each pixel. The time delay  $\tau$  is indicated at the top of each image. The origin of the  $xz$  plane is taken to be consistent with those of Figs. 3–5. The maximum brightness values of the images at  $\tau = -3.50$ ,  $-1.13$ , and  $0$  ps are 1.08, 3.46, and 1.54, respectively, provided that of Fig. 5 is unity. To make each profile clear, however, each image is normalized to its peak value. Lines (c)–(h) reveal the segments along which the profiles are investigated and displayed in Fig. 7.

accidental fluctuations since the observed images are very stable. Then the filaments come together to form a large bundle at around  $\tau = -1.13$  ps. At this stage, the observed pump light seems to be most intense in the sequence of delay steps, and after passing this point the laser energy drops. This is because the pump pulse spends its energy to make a relatively large plasma and furthermore because the plasma induced by the front portion of the pump pulse absorbs and refracts the following pump light [5,20]. We observed that emission from the laser-induced plasma covers the region  $-2 \times 10^2 \mu\text{m} < x < 2 \times 10^2 \mu\text{m}$ ,  $-1.2 \times 10^3 \mu\text{m} < z < 4 \times 10^2 \mu\text{m}$ . At around the vacuum focus, the weakened pulse appears to have some energy-concentrated parts, which cannot be regarded as filaments. The position of the most intense part is slightly different from that in Fig. 3 even with the same delay time. This is because the path of the pump pulse is altered due to the nonlinear properties of the medium [20].

### B. Analysis of instantaneous profiles of light pulses

Now we obtain the instantaneous profiles of light pulses by making use of the relations derived in the preceding section. Although the pump pulse changes its shape as it propagates, we use the relation (13) derived under the assumption of parallel propagation. This assumption is not valid for the overall propagation. However, it can be considered to be reasonable if we consider only the area near the central axis, and a time width of about a few hundreds of femtoseconds, where only the information on this time scale contributes to the conversion result at each point. (This statement was verified by taking consecutive FTOP images at delay times around that of the image to be examined.) The group velocity of the light pulse  $v_g$  is set to that in vacuum  $c$  since the refractive index of helium gas is almost unity and its dispersion is negligible. The probe temporal profile  $G(t)$ , with a FWHM of 95 fs, is assumed to be proportional to the square of the hyperbolic secant. As written in the preceding section, images corresponding to the value of  $\int dy' \hat{I}(x, y', z - v_g \tau - y')$  are obtained by extracting the square root of each pixel after applying a Bayesian deconvolution procedure to the FTOP images. Since the transmittance of the image system, the quantum efficiency of the employed detector, and the value of  $\omega \Delta n_2$  are common throughout all measurements, we can readily discuss the relative values of the instantaneous pump intensity using the images obtained without specifying these values. For convenience, let us define  $V(x, z, \tau)$  as a suitably normalized function proportional to  $\int dy' \hat{I}(x, y', z - v_g \tau - y')$ .

We calculate the value of  $V(x, z, \tau)$  from the images in Figs. 3 and 4. Figures 5 and 6 show images of  $V(x, z, \tau)$  for energy pulses of 0.53 mJ and 13 mJ, respectively. The function  $V(x, z, \tau)$  is normalized with the maximum brightness value of the pixels in Fig. 5 set to unity. The maximum brightness values of the images at  $\tau = -3.50$ ,  $-1.13$ , and 0 ps in Fig. 6 are 1.08, 3.46, and 1.54, respectively. In Figs. 5 and 6, profiles corresponding to small-intensity areas can be observed clearly compared to those in Figs. 3 and 4.

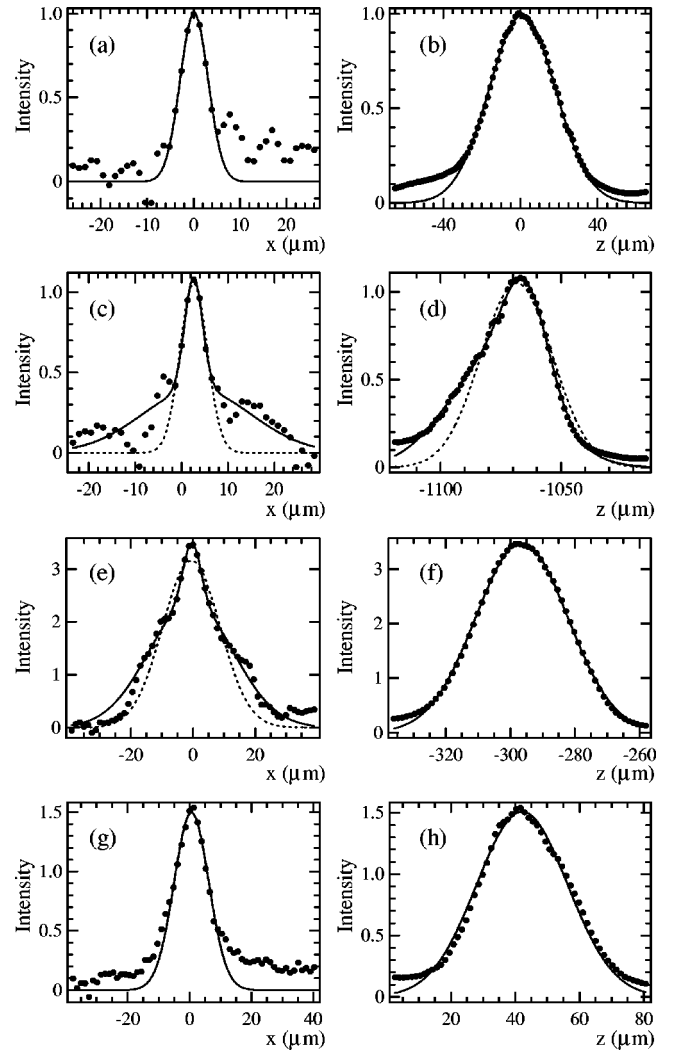


FIG. 7. Profiles along the lines indicated in Figs. 5 and 6. The ordinate and the abscissa of each graph represent the intensity and the position along the line, respectively. The dots correspond to the experimental results, and the solid lines are the approximated curves of the experimental data. The negative values of the experimental results indicate that the pixels have negative values before operating the square root. The fitting is performed before extracting the square root from the deconvoluted images since the square-root procedure gives rise to serious noise level magnifications near the zero value. The intensity profiles are assumed to be of the forms of single Gaussian functions except for lines (c), (d), and (e), along which the intensity profiles are approximated by the sums of two Gaussian functions. For comparison, results of single Gaussian fittings are also shown by the dashed curves in the graphs of these three lines.

To discuss the profiles quantitatively, we extract the value of  $V(x, z, \tau)$  along several lines in the images. Figure 7 shows graphs of intensity distributions along the lines (a)–(h) in Figs. 5 and 6. The ordinate and the abscissa in each graph represent the value of  $V(x, z, \tau)$  at each pixel along the line and the distance, respectively. The dots indicate the experimental data, i.e., the brightness of the pixels in Figs. 5 and 6. Now we should find the regression curve of these points. Since the intensity profile of the pump pulse can

TABLE I. FWHMs of the intensity distributions along the  $x$  and  $z$  axes.

Line	FWHM ( $\mu\text{m}$ )	Line	FWHM ( $\mu\text{m}$ )	Estimated temporal FWHM (fs)
(a)	$7.1 \pm 0.8$	(b)	$40.7 \pm 0.3$	$133.7 \pm 1.5$
(c)	$4.6 \pm 1.2$	(d)	$21.7 \pm 1.1$	$70.9 \pm 4.8$
	$27.7 \pm 3.9$		$46.9 \pm 1.3$	$126.2 \pm 16.6$
(e)	$6.7 \pm 0.9$	(f)	$33.7 \pm 0.2$	$110.1 \pm 1.5$
	$32.0 \pm 0.9$			
(g)	$13.2 \pm 0.5$	(h)	$33.4 \pm 0.5$	$102.2 \pm 2.7$

change from the original one due to nonlinear propagation, it is not easy to identify each profile with a specific function. There are indeed many results obtained by simulating the behaviors of intense pulses propagating in media [2–7,21], but generally these results seem to be very complicated and largely dependent on incidental conditions. At this time, we adopt Gaussian functions for graph fitting only for their simplicity. In the linear case, at least, these functions are commonly used for expressing the cross-section profile and for approximating the temporal profile. To avoid noise level magnifications near the zero value due to the square-root operation, we derive an approximated curve by extracting the square root after applying the least squares method to the square of the brightness in Figs. 5 and 6, which corresponds to  $[V(x,z,\tau)]^2$ . Since lines (c), (d), and (e) cannot be fully approximated by single Gaussian functions, they are approximated by sums of two Gaussian functions; this seems to be a good strategy. Approximated curves are shown in Fig. 7 by the solid lines. For comparison, the results of single Gaussian curves are also shown in (c), (d), and (e) by the dashed lines.

Here, we pay attention to the width of the distribution in particular. The FWHMs of the Gaussian functions along the lines (a)–(h) are summarized in the first four columns of Table I. For lines (c), (d), and (e), the FWHMs of every two Gaussian functions are displayed. The errors are estimated by considering the fitting deviation, the diffraction effect while carrying out imaging, and the finite size of the pixels.

### C. Estimation of temporal widths

At this stage, we can further estimate the temporal width for each instantaneous intensity profile. For this purpose, we define  $\Delta x$  and  $\Delta z$  as the FWHMs of the  $V(x,z,\tau)$  profiles along the  $x$  and  $z$  directions, respectively. We consider it reasonable to assume cylindrical symmetry around the propagation direction and that the distribution along each coordinate axis is independent of the other. This means that the intensity distribution of each profile along the  $y$  direction is also approximated by a Gaussian with a FWHM of  $\Delta x$ . Although several filaments can be seen in the image of  $\tau = -3.50$  ps in Fig. 6, each of them is assumed to be symmetric around its central axis. Hence, if we pick only one of the filaments, the image is treated as if it were a single-filament image. However, since the filaments directed at a slant may not retain the precision of the image conversion (because of the failure in the parallel propagation assumption), we consider only the filament at the center. Under this approxima-

tion, therefore, the function  $\int dy' \hat{I}(x,y',z-v_g\tau-y')$  is the product of the  $x$  profile and a function that is the convolution of the  $y$  and  $z$  profiles. Hence, the estimated width of the  $z$  profile of  $\hat{I}(x,y,z)$  can be derived from  $\sqrt{(\Delta z)^2 - (\Delta x)^2}$ . As for the double Gaussian profiles, we consider each case separately. Along lines (c) and (d), shorter widths are paired, and longer ones are also paired. Along lines (e) and (f), on the other hand, we judge from the image that the larger width of (e) gives a distribution of a wide region of intensities, and therefore do not take this width into account.

The estimated  $z$  widths of  $\hat{I}(x,y,z)$  are also described in terms of the temporal width in the rightmost column of Table I. The errors are estimated only from those of  $\Delta x$  and  $\Delta z$ . If we consider the case that the cylindrical symmetry assumption is seriously broken, the errors should be multiplied by factors of 2 or 3 excluding the upper row of (d). [The error of the upper row of (d) from the breaking of the symmetry assumption is not significant compared with that described in Table I.] In any case, the instantaneous temporal width values in the middle of the propagation are almost the same as at incidence.

### D. Discussion of the results

We briefly discuss the behaviors of the optical pulses by taking the estimated widths into account.

First, let us consider the case of a 0.53-mJ pulse. The FWHM along line (a) corresponds to that of the cross section at the beam waist, which is 4.3 times as large as that of the cross section at the ideal focusing plane of the Gaussian beam. This is considered to be due to an aberration of the pump pulse focusing system rather than a nonlinear effect or plasma generation. However, the temporal width is not so significantly elongated compared to that at incidence; the ratio between the widths is 1.4. Hence, the intensity at the focal point seems to be only about 0.039 times as large as that of the ideal case.

Next, let us consider the 13-mJ case. At  $\tau = -3.50$  ps, the pulse has split into several filaments, and at least the central one has fine structure, that is, it includes two components. The temporal width of one component is less than the incident pulse width. The distance between the two peaks of the Gaussians along the  $z$  axis on the image plane is  $12.4 \pm 2.3 \mu\text{m}$ , which corresponds to  $41.4 \pm 7.7$  fs in terms of the temporal distance, and this is less than the  $x$  width of the other component. Therefore, even if the intensity peaks are separated along the  $y$  direction instead of the  $z$  direction in

real three-dimensional space, the two components cannot be isolated. Of course, this kind of phenomenon is widely known as the self-modulation of an intense pulse [4–6,21,22], and our result corresponds to direct observation of this effect for femtosecond pulses in the middle of the propagation. (We have observed this kind of modulation under several other conditions also, and we should therefore proceed to take systematic data in the future.) In any case, this result supports the assertion that FTOP can separately investigate each filament profile (even along the propagation axis) at a specific instant. At around  $\tau = -1.13$  ps, although the filaments are concentrated into a bundle, the temporal widths are not considerably changed. No fine structure is observed in the bundle; this is considered to be due to the averaging of the structures of the numerous filaments. At  $\tau = 0$  ps, the pulse energy is significantly reduced to about 1.2 mJ, which can be roughly estimated by comparing the maximum brightness and the width of the distribution between Figs. 5 and 6. The peak position is displaced about  $41.1 \pm 1.0 \mu\text{m}$  from that in Fig. 5, almost completely along the  $z$  direction in the images. This displacement is considered to be along the  $y$  direction in real three-dimensional space, because any displacement in the positive direction along the  $z$  axis would mean that the pulse travels faster than in vacuum, which is physically impossible with the exception of some special cases [23]. It is also remarkable that the cross section is undoubtedly larger than that in the 0.53-mJ case. We confirmed that the widths of the cross sections showed similar values at other delay times around  $\tau = 0$  ps under 13-mJ incident energy. This finding implies that the nonabsorbed components of the pulse have also suffered from diffraction or refraction due to some kind of nonlinear effect. These alterations of the pulse profile at this instant are considered to reflect the influence of nonlinearities, such as the optical Kerr effect, plasma generation, and refraction or absorption by the induced plasma [5,20,24].

Lastly, we add the estimation of the upper limit of the phase difference between the  $x$  and  $z$  components of the probe's electric field under our experimental conditions, making use of a reported  $n_2$  value of helium gas for 800-nm light, which is  $3.5 \times 10^{-21} \text{ cm}^2/\text{W}$  at 1 atm and room temperature [17]. Before proceeding to the estimation, we note that the largest value of the phase difference occurs at the focal point. Provided that there is no loss of pump pulse energy, the intensity at the focal point is estimated to be  $6.5 \times 10^{15} \text{ W}/\text{cm}^2$  in the 0.53-mJ case by using the values in the first row of Table I. Hence, the nonlinear index change is

$2.3 \times 10^{-5}$  at this point. We approximate  $\Delta n_2 \sim n_2$ , and get  $(\omega \Delta n_2 / 2c) \int I(\mathbf{r}', t(\mathbf{r}')) dy' \sim 6.6 \times 10^{-4}$ . Furthermore, even if the 13-mJ pulse did not lose its energy, the phase difference would be only  $1.1 \times 10^{-2}$  at the focal point. These values, although greatly overestimated, are small enough to guarantee the approximation in Eq. (7).

As described above, it is clear that FTOP has succeeded in direct investigation of the propagation of intense femtosecond optical pulses, especially in estimation of the instantaneous profile along the propagation axis.

## V. SUMMARY

We observed instantaneous profiles of intense femtosecond laser pulses propagating in helium gas, and reconstructed images corresponding to the instantaneous intensity distributions by using relations derived under suitable approximations. In particular, we estimated the temporal pulse width of the femtosecond pulse at each instant of time. This method makes it feasible to investigate each filament in a multifilament structure even along its propagation axis.

Since a profile can be observed only through projection, we cannot resolve the real three-dimensional distribution at this time. This difficulty would be overcome by performing observations along every direction in the plane perpendicular to the pump propagation axis, which is in fact very hard to do.

Possible applications of this method include high-power pulse monitoring for space and time. Furthermore, quantum-mechanical treatment may produce other aspects of this method, e.g., quantum nondemolition measurements concerning photon numbers with partial space and time resolution. Measurements with coupling between space and time coordinates might show us an interesting uncertainty relation. Although certain materials are needed to visualize a light profile at the present time, light propagation even in vacuum can be seen if the light is made intense enough to induce the third nonlinear effect of the vacuum sufficiently.

## ACKNOWLEDGMENTS

The authors would like to thank Y. Suzuki and T. Hiruma for their support, and T. Urakami for his helpful discussions. Part of this study was performed thanks to Special Coordination Funds for promoting the Ministry of Education, Culture, Sports, Science and Technology of the Japanese Government.

- 
- [1] H.R. Lange, G. Grillon, J.-F. Ripoche, M.A. Franco, B. Lamouroux, B.S. Prade, and A. Mysyrowicz, *Opt. Lett.* **23**, 120 (1998).  
 [2] A. Braun, G. Korn, X. Liu, D. Du, J. Squier, and G. Mourou, *Opt. Lett.* **20**, 73 (1995).  
 [3] A. Pukhov and J. Meyer-ter-Vehn, *Phys. Rev. Lett.* **76**, 3975 (1996).  
 [4] S.L. Chin, A. Brodeur, S. Petit, O.G. Kosareva, and V.P. Kan-

- didov, *J. Nonlinear Opt. Phys. Mater.* **8**, 121 (1999).  
 [5] P. Chessa, E. De Wispelaere, F. Dorchie, V. Malka, J.R. Marquès, G. Hamoniaux, P. Mora, and F. Amiranoff, *Phys. Rev. Lett.* **82**, 552 (1999).  
 [6] O.G. Kosareva, V.P. Kandidov, A. Brodeur, C.Y. Chien, and S.L. Chin, *Opt. Lett.* **22**, 1332 (1997); O.G. Kosareva, V.P. Kandidov, A. Brodeur, and S.L. Chin, *J. Nonlinear Opt. Phys. Mater.* **6**, 485 (1997); M. Mlejnek, E.M. Wright, and J.V.

- Moloney, *Opt. Lett.* **23**, 382 (1998); *Phys. Rev. E* **58**, 4903 (1998); *IEEE J. Quantum Electron.* **35**, 1771 (1999); N. Aközbek, C.M. Bowden, A. Talebpour, and S.L. Chin, *Phys. Rev. E* **61**, 4540 (2000).
- [7] M. Mlejnek, M. Kolesik, J.V. Moloney, and E.M. Wright, *Phys. Rev. Lett.* **83**, 2938 (1999); A. Chiron, B. Lamouroux, R. Lange, J.-F. Ripoche, M. Franco, B. Prade, G. Bonnaud, G. Riazuelo, and A. Mysyrowicz, *Eur. Phys. J. D* **6**, 383 (1999).
- [8] M. Fujimoto, S. Aoshima, M. Hosoda, and Y. Tsuchiya, *Opt. Lett.* **24**, 850 (1999); S. Aoshima, M. Fujimoto, M. Hosoda, and Y. Tsuchiya, in *High-Power Laser Ablation II*, Proceedings of SPIE, Osaka, Japan, 1999, edited by C. R. Phipps and M. Niino (SPIE, Bellingham, WA, 2000), Vol. 3885, p. 461.
- [9] R. W. Boyd, *Nonlinear Optics* (Academic Press, San Diego, 1992).
- [10] P.D. Maker and R.W. Terhune, *Phys. Rev.* **137**, A801 (1965).
- [11] R.W. Hellwarth, *Prog. Quantum Electron.* **5**, 1 (1977).
- [12] R. L. Sutherland, *Handbook of Nonlinear Optics* (Marcel Dekker, Inc., New York, 1996).
- [13] M. Born and E. Wolf, *Principles of Optics*, 7th ed. (Cambridge University Press, Cambridge, 1999).
- [14] T.J. Kennett, W.V. Prestwich, and A. Robertson, *Nucl. Instrum. Methods* **151**, 285 (1978).
- [15] D. McMorrow, W.T. Lotshaw, and G.A. Kenney-Wallace, *IEEE J. Quantum Electron.* **24**, 443 (1988).
- [16] J.-F. Ripoche, G. Grillon, B. Prade, M. Franco, E. Nibbering, R. Lange, and A. Mysyrowicz, *Opt. Commun.* **135**, 310 (1997).
- [17] E.T.J. Nibbering, G. Grillon, M.A. Franco, B.S. Prade, and A. Mysyrowicz, *J. Opt. Soc. Am. B* **14**, 650 (1997).
- [18] T. Hattori and T. Kobayashi, *J. Chem. Phys.* **94**, 3332 (1991).
- [19] A. Brodeur, F.A. Ilkov, and S.L. Chin, *Opt. Commun.* **129**, 193 (1996); H. Schillinger and R. Sauerbrey, *Appl. Phys. B: Lasers Opt.* **68**, 753 (1999).
- [20] P. Monot, T. Auguste, L.A. Lompré, G. Mainfray, and C. Manus, *J. Opt. Soc. Am. B* **9**, 1579 (1992).
- [21] A.A. Zozulya, S.A. Diddams, A.G. Van Engen, and T.S. Clement, *Phys. Rev. Lett.* **82**, 1430 (1999).
- [22] J.K. Ranka, R.W. Schirmer, and A.L. Gaeta, *Phys. Rev. Lett.* **77**, 3783 (1996); S.A. Diddams, H.K. Eaton, A.A. Zozulya, and T.S. Clement, *Opt. Lett.* **23**, 379 (1998).
- [23] L.J. Wang, A. Kuzmich, and A. Dogariu, *Nature (London)* **406**, 277 (2000).
- [24] S.C. Rae, *Opt. Commun.* **97**, 25 (1993); V.P. Kandidov, O.G. Kosareva, and S.A. Shlenov, *Kvant. Elektron.* **21**, 971 (1994) [*Quantum Electron.* **24**, 905 (1994)].